Hassanzadegan, A., Zimmermann, G. (2014): A Poroelastic Description of Permeability Evolution. - *Pure and Applied Geophysics*, *171*, 7, p. 1187-1201.

DOI: http://doi.org/10.1007/s00024-013-0714-6

A poroelastic description of permeability evolution

Alireza Hassanzadegan and Günter Zimmermann[1]

[1]Helmholtz Centre Potsdam (GFZ), German Research Centre for Geosciences, Telegrafenberg, 14473, Potsdam, Germany

02 October 2013

Abstract

The pore pressure changes, due to injection and production of water into a geothermal reservoir, result in changes of stress acting on reservoir rock and consequently changes in mechanical and transport properties of the rock. The bulk modulus and permeability were measured at different pressures and temperatures. An outcropping equivalent of Rotliegend reservoir rock in North German Basin (Flechtinger sandstone) was employed to perform hydrostatic tests and steady state fluid flow tests. Permeability measurements were carried out while cycling confining pressure at a constant downstream pressure of 1 MPa

where the stress dependence of permeability was determined. Meanwhile the temperature was increased stepwise from 30 °C to 140 °C. The crack porosity was calculated at various temperatures. While the pore volume changes of the cracks are not significant but control fluid flow pathways and consequently the permeability of the rock. A new model was derived which relates the microstructure of porosity, stress-strain curve and permeability. The porosity change was described by the first derivative of stress-strain curve and permeability evolution was ascribed to crack closure and was related to the second derivative of strain-stress curve. The porosity and permeability of Flechtinger sandstone decreased by increasing the effective pressure and after each pressure cycle.

1 Introduction

There is a long-standing interest in understanding the interrelation between deformation and transport properties of porous rock in civil and reservoir engineering. The prediction of production rates and reservoir performance rely on the accurate representation of the poromechanical behavior, where the pore pressure in concert with rock deformation will influence the rock permeability. The reservoir and surrounding rocks deform and change in shape and volume when they are subjected to stress changes. The stresses acting on the reservoir rock will be modified while injecting cold water into reservoir due to changes in pore pressure and temperature. These stress

changes could be accompanied by changes in pore geometry and interconnectivity between pores, and consequently how easily fluid flows through the reservoir rock (permeability). Among reservoir rock properties, permeability is quite challenging as it varies more than 11 orders of magnitudes for different rock types and stress conditions (Brace, 1980). The porosity of the rock is the other important property which controls to a large extent the permeability and effective elastic properties of the crustal rock (Hassanzadegan et al., 2013). The porosity-permeability relationship can be described by principles of hydrodynamics (Bear, 1988) and the porosity changes due to changes in effective pressure and drained bulk modulus can be described by poromechanics (Carroll, 1980).

The poromechanical behavior of the rock includes both elastic and inelastic deformations. Biot (1941, 1956, 1973); Rice and Cleary (1976) derived the constitutive equations that govern the elastic behavior of the saturated porous rock. In measuring the elastic moduli of granular rocks, one may encountered the problem of nonlinearity in stress-strain curves which can be assigned to the opening and closure of the cracks (Walsh, 1980). The crack porosity decreases and bulk modulus (first derivative of stress-strain curve) increases with increasing effective pressure (Hassanzadegan et al., 2013). To account properly for the effect of nonlinearity, the second derivative of stress-strain curve (bulk modulus derivative) should also being considered. A common approach is to relate the second derivative of stress-strain curve to porosity microstructure by a set of statistical distribution functions, the

aspect ratios distribution functions of penny-shaped cracks (Walsh, 1980). If the population of penny-shaped cracks is defined the porosity and permeability could be correlated and the permeability evolution could be estimated (Guéguen and Dienes, 1996). Morlier (1971) developed a method to relate strain to detailed description of pore geometry at the microscale and provided the distribution functions of porosity microstructure.

The stress dependence of permeability and its relation to pore geometry have been studied experimentally and analytically (Zoback and Byerlee, 1975; Bernabe, 1986, 1987; David et al., 1994). Bernabe (1986, 1987) observed a large hysteresis in permeability at loading and unloading paths for different rock types. David et al. (2001) reported a rapid reduction in permeability evolution between 15 to 40 MPa which was assigned to the closure of the cracks. Guéguen et al. (1996) assigned the pressure dependence of permeability of cracked rocks to elastic closure of cracks and crack roughness, where the cracks are compliant and close easily compared to rounded pores. A comprehensive and quantitative analysis of the influence of pore space topology on permeability is given by Sarout (2012) in terms of pores/cracks characteristic size, geometry and connectivity.

The permeability of the rock is a macroscopic concept where its mathematical description requires that detailed description of pore geometry to be well-defined. The aim of this study is to connect the permeability evolution to the changes in porosity microstructure (elastic deformation of penny-shaped cracks). It results to a new analytical model which interrelates the evolution

of permeability with microstructure of porosity and bulk elastic modulus. The permeability of the rock will be modified when crack like pores experience an elastic deformation. That is, the fraction of the cracks that are hydraulically connected and provide pathways to fluid flow will change due to applied effective pressure. The new permeability model is characterized by spherical pores and penny-shaped cracks, imbedded into a solid phase. The permeability model assumes that spherical pores are connected by cracks.

2 Theoretical background

The poroelastic theory assumes a quasi static deformation where the state variables (temperature, pressure, etc.) are in thermodynamic equilibrium. However, if the state variables vary with time the system undergoes a process. The number of state variables required to characterize a process might be larger than thermodynamic equilibrium, for example in describing the fluid flow in porous media, viscosity and permeability are required. Viscosity is a physical property of the fluid and permeability is a property of porous media.

2.1 Permeability

Permeability is a transport property which allows to quantify the fluid flow in porous media and is a measure of how easily fluid flows through a rock (Guéguen et al., 1996). Furthermore, permeability is a measure of the geometry of the pores (pore dimension) and their interconnections (Brace, 1978).

It is the intricate relation between the pore geometries and their interconnectivity which makes the permeability modeling in terms of microstructure a challenging task (Sarout, 2012).

Bear (1988) described the conceptual models employed to derive Darcy's law:

$$q = -\frac{k}{\eta}\nabla(P_p - \rho_f g z) \tag{1}$$

where ∇ is a vector differential operator (gradient). z is the vertical distance and points downward. The proportionality constant $\frac{k}{\eta}$, mobility, includes the fluid viscosity η and intrinsic permeability k. q is the fluid flux vector,g is the gravity acceleration and ρ_f is fluid density. If the fluid density considered to be constant, a potential energy function $\varphi = \frac{P_p}{\rho} - gz$, energy per unit mass of the fluid, can be defined such that

$$q = -(\frac{k\rho_f}{\eta})\nabla\varphi \tag{2}$$

A general relation between porosity and permeability is given by Bear (1988):

$$k = f(s)f(\phi)R^2 \tag{3}$$

where $f(s)$ is a shape function, $f(\phi)$ is a porosity function and R is a hydraulic radius defined as cross sectional area divided by wetted perimeter (Sisavath et al., 2000). The Kozeny-Carman permeability (Carman, 1956) was derived by employing Hagen-Poiseuille equation for steady laminar flow through a

bundle of capillary tubes where the permeability can be expressed in terms of porosity ϕ, specific surface area S or a flow path characteristic length d, and tortuosity τ :

$$k = \frac{c\phi^3}{\tau^2 S^2} \tag{4}$$

where c is a geometric factor. The specific surface area, the pore surface per bulk volume of porous media, is a dominant parameter in permeability models which contributes in shape factor. A particular extension of this equation is to consider a packed bed of spheres with $S = \frac{3}{2}\frac{1-\phi}{d}$ and $\tau = 1$, which results in:

$$k = c_1 \frac{\phi^3}{(1-\phi)^2} d^2 \tag{5}$$

where c_1 includes the geometric factor and the factor of $(\frac{3}{2})^2$. The assumption $\tau = 1$, laterally states that all the pores are part of a connected network (infinite path).

2.2 Poroelasticity

The key concepts in poroelasticity theory underly the following equations, describing the evolution of two kinematic quantities: bulk strain of the porous rock ε_b and change in fluid mass content m in terms of their conjugate dynamic quantities, confining pressure P_c and pore pressure P_p (Detournay and

Cheng, 1993):

$$\varepsilon_b = \frac{P_c - \alpha P_p}{K_d} \tag{6a}$$

$$m - m_0 = -\frac{\alpha \rho_0}{K_d}\left[P_c - \frac{1}{B}P_p\right] \tag{6b}$$

B and α are Skempton and Biot coefficients, respectively. K_d is drained bulk modulus and ρ_0 is fluid density at reference condition. These two equations describe the fluid rock interaction under quasistatic conditions for a representative elementary volume (REV). That is, an increase in pore pressure dilates the rock, an increase in fluid mass content causes a rise in pore pressure and the fluid mass content decreases due to applied pressure which results in volume compression (Detournay and Cheng, 1993). The inertial forces and other high frequency effects are neglected and it is assumed that the characteristic length of REV is much larger than pore scale. The poroelasticity theory describes the porosity changes in terms of the drained bulk modulus and effective pressure (Carroll and Katsube, 1983) :

$$d\phi = -\left(\frac{1-\phi_0}{K_d} - \frac{1}{K_s}\right) dP' \tag{7}$$

where $P' = P_c - P_p$ is Terzaghi effective pressure and ϕ_0 is initial porosity. The Eq. 7 states that porosity decreases with increasing effective pressure and the rate of porosity change with pressure is inversely proportional to drained bulk modulus. That is, the modification of porosity is related to

drained bulk modulus. In addition, it is quite common to ascribe the non-linearity in bulk modulus and its pressure-dependence to porosity change and crack closure (Walsh, 1980). Accordingly, the change in porosity and nonlinearity in bulk modulus can be linked together.

2.3 Crack closure and porosity

In a porous rock, the bulk modulus is no longer equal to the bulk modulus of solid grains K_s but is a function of porosity ϕ. Walsh (1965) derived the effective bulk modulus of the rock in terms of the bulk modulus of solid phase K_s and the rate of change in porosity with external pressure. For a two phase porous rock which is consisted of penny shaped cracks imbedded into the solid phase, the effective bulk modulus of the porous media K_d was derived by Walsh (1965) to be:

$$K_d = K_s / \left[1 + \left(\frac{16}{9}\right)\left(\frac{1-\nu_s^2}{1-2\nu_s}\right)\sum \frac{c^3}{V_b}\right] \tag{8}$$

where ν_s is the Poisson's ratio of the solid grains and V_b is the bulk volume. The summation in Eq.8 is over all open cracks. The aspect ratio of penny-shaped (oblate spheroid) cracks, $a = b/c$ with $b << c$, contains the microstructural information of the pore geometry, with semi minor axis b (crack aperture) and semi major axis c (crack radius).

The change in aperture of a 2D-penny shaped crack can be derived by

elasticity theory (Walsh, 1965):

$$b = b_0 \left[1 - \frac{2(1-\nu_s^2)}{aE} P\right] \tag{9}$$

where E is the Young's modulus. The Eq.9 suggests that a penny-shaped crack of initial aspect ratio $a_0 = b_0/c_0$ will fully close when pressure reaches a closure pressure $P^*_{2D} = aE/(2(1-\nu_s^2)$.

Having the hydrostatic compression test performed, the initial crack porosity and crack porosity change can be calculated from deviation of bulk volumetric strain from the volumetric strain of the solid matrix (Walsh, 1965):

$$\Delta\phi_c = \frac{\Delta V_c}{V_b} = \int \frac{1}{K_d} dP' - \int \frac{1}{K_s} dP' = \varepsilon_b(P') - \varepsilon_s(P') \tag{10}$$

The crack porosity at each pressure level, less than that required to close all the cracks, can be calculated by determining how many is closed in passing through each pressure level. Morlier (1971) developed a method to derive the aspect ratio distribution function where the crack density whose initial aspect ratio lies between a and $a + da$ is given by $d\Gamma(a) = -\gamma(a)da$. $\gamma(a)$ and $\Gamma(a)$ represent the aspect ratio distribution function and the cumulative distribution function of open cracks, respectively.

$$\gamma(a) = -\frac{d\Gamma(a)}{da} = \frac{-3}{4\pi} \left[\frac{3\pi K_s(1-2\nu_s)}{4(1-\nu_s^2)}\right]^2 \left[\frac{d^2V}{dP^2}\right]_{P^*} \tag{11}$$

where the derivative $\left[\frac{d^2V}{dP^2}\right]_{P^*}$ should be evaluated at the crack closing

pressure P^*:

$$P^* = \left[\frac{3\pi a K_s(1-2\nu_s)}{4(1-\nu_s^2)}\right] \tag{12}$$

P^* describes the closing pressure of a three-dimensional penny shaped crack of initial aspect ratio a.

Zimmerman (1991) proposed an exponentially decreasing function for evolution of bulk modulus (first derivative of strain-stress curve):

$$\frac{1}{K_d} = \frac{1}{K_d^\infty} + \left[\frac{1}{K_d^i} - \frac{1}{K_d^\infty}\right] \exp(-\frac{P'}{\hat{P}}) \tag{13}$$

where $\hat{P}$ is a characteristic closure pressure corresponding to an aspect ratio at the maximum of $\gamma(a)$. The peak of $\gamma(a)$ represents the cracks with a higher population. The superscript i refers to relaxed state at low effective pressures and the superscript ∞ refers to confined state at high effective pressures. The second derivative of strain-stress curve can be derived by differentiation of Eq.13 with respect to pressure at corresponding closing pressure (Eq.12). Inserting the second derivative in Eq.11 leads to:

$$\gamma(a) = \left[\frac{9K_s(1-2\nu_s)}{16\hat{a}(1-\nu_s^2)}\right] \left[\frac{1}{K_d^i} - \frac{1}{K_d^\infty}\right] \exp(-\frac{a}{\hat{a}}) \tag{14}$$

where $\hat{a}$ is the characteristic aspect ratio evaluated at $\hat{P}$.

Thus, the crack porosity function can be written as:

$$C(a) = \frac{d\phi}{da} = \frac{4\pi a}{3}\gamma(a) = \left[\frac{3\pi K_s(1-2\nu_s)}{4(1-\nu_s^2)}\right]\left[\frac{1}{K_d^i} - \frac{1}{K_d^\infty}\right]\frac{a}{\hat{a}}\exp(-\frac{a}{\hat{a}}) \quad (15)$$

Consequently, the crack porosity can be calculated by the following formula (Jaeger et al., 2007):

$$\phi_{crack} = \int_0^\infty C(a)da = \left(\frac{1}{K_d^i} - \frac{1}{K_d^\infty}\right)\hat{P} \quad (16)$$

The correlation between porosity and permeability requires that a detailed description of pore geometry at micro scale is given. The following section describes a new permeability model which relates the permeability of porous medium to its microstructure through evolution of bulk modulus.

3 Permeability modeling

The permeability of the rock is a macroscopic concept defined at a Representative Elementary Volume (REV). The mathematical description of permeability requires that microstructure of the porosity to be well-defined. According to Scheidegger (1974), Guéguen and Dienes (1996) the porosity and permeability could be correlated if the microstructure of the porosity is described by a set of statistical distribution functions that describe pore geometry and pore size distribution. The pore geometry can be divided roughly into two categories: equant pores and cracks. Albeit, there is no clear di-

vision between these two categories. The low aspect ratio pores at grained contacts can be viewed as crack porosity and the high aspect ratio pores may represent the equant pores. In granular materials such as sandstone, both equant pores and cracks coexist.

Bernabe (1986) assumed that permeability k is a single valued function of P_c and P_p. It was assumed that the knowledge of permeability as a function of confining pressure and zero pore pressure is enough to predict the value of permeability at any pair of (P_c, P_p) and effective pressure P_{eff} was defined as confining pressure that would result in the same permeability $k(P_{eff}) = k(P_c, 0)$. If the effective pressure defined as a linear combination of P_c and P_p, the $k(P_c, P_p)$ would be a family of curves that can be approximated by parallel straight lines. Bernabe (1986) suggested a differential form of the permeability evolution:

$$dk = \left(\frac{\partial k}{\partial P_c}\right)_{P_p} dP_c + \left(\frac{\partial k}{\partial P_p}\right)_{P_c} dP_p \tag{17}$$

Here, the permeability would be approximated as a function of Terzaghi effective pressure:

$$k(P') = k(P^\infty) - \int_{P'}^{P^\infty} \left(\frac{\partial k}{\partial P'}\right)_T dP' = k(P^\infty) - \int_{P'}^{\infty} \left(\frac{\partial k}{\partial \phi}\right)\left(\frac{\partial \phi}{\partial P'}\right) dP' \tag{18}$$

where $k(P^\infty)$ is high-pressure permeability where all the cracks are closed and subscript T represents a constant temperature. The porosity depen-

dence of permeability can be derived by employing Kozeny-Carman equation (Eq.5):

$$\frac{dk}{d\phi} = c_1 d^2 (3e^2 + 2e^3) \tag{19}$$

where e is the void ratio defined as $e = \frac{\phi}{1-\phi}$. It is assumed that porosity dependence of permeability $\frac{dk}{d\phi}$ is governed by equant pores and is independent of pressure, therefore can be taken out of the integral. The assumption that pressure dependence of porosity is governed by cracks requires that $\frac{\partial \phi}{\partial P'}$ is given by Eq.7. Inserting Eq.7 in Eq.18 leads to:

$$k(P') = k(P^\infty) + \left(\frac{\partial k}{\partial \phi}\right) \int_{P'}^{P^\infty} \left(\frac{1-\phi_0}{K_d} - \frac{1}{K_s}\right) dP' \tag{20}$$

and if the tangent drained bulk modulus is estimated by Eq.13, the following equation would be obtained:

$$\begin{aligned} k(P') = k(P^\infty) &+ \left(\frac{\partial k}{\partial \phi}\right) \int_{P'}^{P^\infty} \left(\frac{(1-\phi_0)}{K_d^\infty} - \frac{1}{K_s}\right) dP' \\ &+ \left(\frac{\partial k}{\partial \phi}\right) \int_{P'}^{P^\infty} (1-\phi_0) \left(\frac{1}{K_d^i} - \frac{1}{K_d^\infty}\right) \exp\left(-\frac{P'}{\hat{P}}\right) dP' \end{aligned} \tag{21}$$

The integration of definite integral leads to:

$$k(P') = k(P^{\infty}) + \left(\frac{\partial k}{\partial \phi}\right)\left(\frac{(1-\phi_0)}{K_d^{\infty}} - \frac{1}{K_s}\right)(P^{\infty} - P') + \left(\frac{\partial k}{\partial \phi}\right)\hat{P}(1-\phi_0)\left(\frac{1}{K_d^{i}} - \frac{1}{K_d^{\infty}}\right)\left[\exp\left(-\frac{P'}{\hat{P}}\right) - \exp\left(-\frac{P^{\infty}}{\hat{P}}\right)\right] \tag{22}$$

where P^{∞} is a sufficiently high pressure at which the confined bulk modulus K_d^{∞} is obtained. The confined state pressure P^{∞} describes the maximum effective pressure at which the elastic deformation of cracks may occur. Thus, the only unknown parameters in Eq.22 are $\left(\frac{\partial k}{\partial \phi}\right)$ and $k(P^{\infty})$ or simply the Kozeny-Carman term $c_1 d^2$ and high-pressure permeability $k(P^{\infty})$. Rewriting of Eq.22 in terms of scaled pressure $\left(\frac{P'}{\hat{P}}\right)$ as an independent variable results in:

$$\begin{aligned} k(P') = k(P^{\infty}) &+ \left(\frac{\partial k}{\partial \phi}\right)\hat{P}\left(\frac{(1-\phi_0)}{K_d^{\infty}} - \frac{1}{K_s}\right)\left(\frac{P^{\infty}}{\hat{P}}\right) \\ &- \left(\frac{\partial k}{\partial \phi}\right)\hat{P}\left(\frac{1}{K_d^{i}} - \frac{1}{K_d^{\infty}}\right)(1-\phi_0)\exp\left(-\frac{P^{\infty}}{\hat{P}}\right) \\ &+ \left(\frac{\partial k}{\partial \phi}\right)\hat{P}\left(\frac{1}{K_d^{i}} - \frac{1}{K_d^{\infty}}\right)(1-\phi_0)\exp\left(-\frac{P'}{\hat{P}}\right) \\ &- \left(\frac{\partial k}{\partial \phi}\right)\hat{P}\left(\frac{(1-\phi_0)}{K_d^{\infty}} - \frac{1}{K_s}\right)\left(\frac{P'}{\hat{P}}\right) \end{aligned} \tag{23}$$

where the first three terms on the right hand side of the Eq.23 are independent of pressure, however the fourth and fifth terms are nonlinear and linear functions of effective pressure, respectively.

4 Material and methods

In order to describe the fluid flow in a poroelastic medium, it is essential to provide the relationships between microstructure of the porosity and strain, and between strain and permeability. The permeability model developed in section 3 represents the pore volume as a combination of spherical pores and cracks. The spherical pores are connected by penny-shaped cracks and the inter-connectivity between them is controlled by elastic closure of cracks. The crack closure mainly influences in fluid pathways (tortuosity), and consequently permeability. While the crack closure theory provide the relation between microstructure of porosity (aspect ratio distribution) and strain, the poroelasticity theory characterizes the relation between strain and applied effective pressure.

In the following, first the hydrostatic tests carried out will be explained where the stress-strain curves not only characterize the bulk behavior of the rock, but also provide valuable information about the microstructure of porosity.

4.1 Sample material and setup

The experiments were carried out on two cylindrical core samples of Flechtinger sandstone, having 50 mm diameter and 100 mm length. It is a Lower Permian (Rotliegend) sedimentary rock in the North German Basin. Flechtinger sandstone is a fine layered sandstone mostly composed of quartz, feldspar and

carbonates. A convectional triaxial test system was employed to perform the experiments (Fig.1). The set up is composed of a confining pressure intensifier to fill and pressurize the triaxial cell up to 140 MPa, a set of Quizix pumps which are operating independently and can increase the pore fluid pressure up to 70 MPa, and a data monitoring and acquisition system. The circumferential and axial extensometers measured the lateral and axial strains. The confining pressure was measured by fluid pressure transducers in triaxial. The pore fluid pressure was measured by pressure transducers in drained experiments and by a differential pressure transducer in permeability tests.

4.2 Experimental procedure, analysis and corrections

The pressure drop was measured at a steady state condition and a constant flow rate of 0.02 ml/min was applied. An extra differential pressure transducer was installed to measure the pressure difference between upstream and downstream through a bypass connection where the frictional pressure drop in capillaries was reduced (see Fig.1).

First, the initial porosity of the samples were determined by imbibition and Archimedes methods. The samples were dried in the 60 °C for 24 hours. Afterwards, the samples were saturated by first applying vacuum to the samples, which were placed in a desiccator and then by drawing water into desiccator where the water imbibes into the porous rock. The initial porosity was calculated by measuring dry weight (W_d), the saturated weight in air (W_s), and the suspended (Archimedes) weight in water (W_a) to be

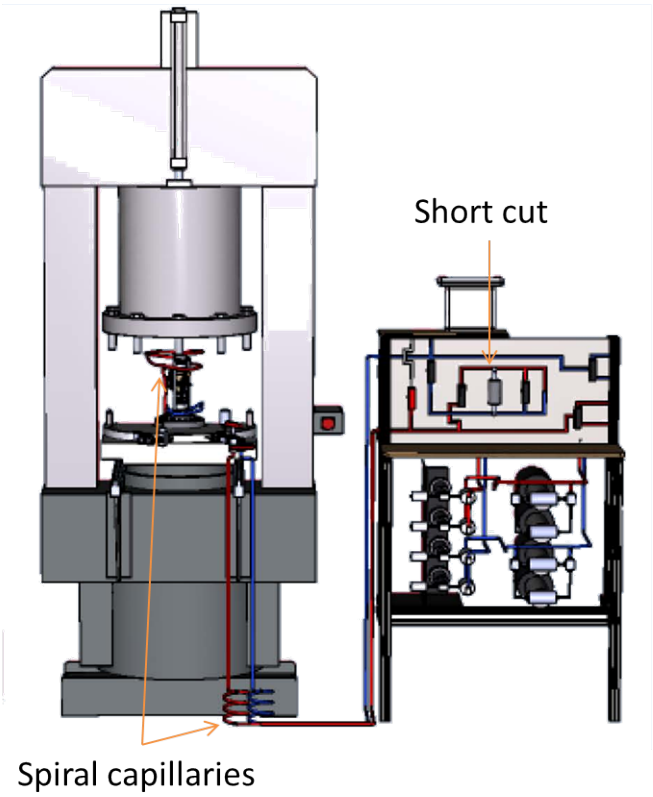

Figure 1: experimental set up: a conventional triaxial cell.

$\phi_0 = (W_s - W_d)/(W_s - W_a)$. Then the sample was mounted in the triaxial cell and the whole system was vacuumized. The vacuumized pressure in the whole set up was monitored to be sure that all the fittings and capillaries are well isolated and there is no leakage. Afterwards, the sample was saturated by flowing water through it for at least 72 hours. The samples were subjected to a cyclic seasonings (preconditioning) to minimize hysteresis and inelastic effects. The preconditioning was composed of four pressure cycles between 0 to 60 MPa with a rate of 1 MPa/min. Two different kind of ex-

periments were carried out on the given specimens (table 1), a hydrostatic drained test (FLG05, where FLG stands for Flechtinger sandstone) and a permeability measurement test (FLG06). The confining pressure was cycled from 2 to 55 MPa and temperature was increased step-wise from 30 °C to 140 °C. The range of experimental pressure and temperature were chosen such that representing changes due to injection of water into a geothermal reservoir in North German Basin (Hassanzadegan et al., 2011). During the injection of cold water into a doublet geothermal reservoir, effective pressure and temperature are chaining. The cold water of 60 °C will be injected into a 145 °C reservoir and the cold thermal front will propagate through the reservoir towards the production well. The effective pressure becomes more compressive in the vicinity of production well due to a decrease in pore pressure and becomes more tensile around the injection well due to an increase in pore pressure. The pore pressure and downstream pressure were held at a constant pressure of 1 MPa at drained and permeability tests, respectively.

Table 1: Specimen properties and achieved experiments

	Experiment	Porosity	Grain density
Specimen	Type	[%]	[gr/cm^3]
FLG05	drained	10.75	2.66
FLG06	permeability	10.68	2.64

Data was recorded every 15 seconds which corresponds to 25 KPa increase in confining pressure. The same sampling rate (four per minute) was employed for the pump system. In order to minimize the effect of small fluc-

tuations of the recorded data two approaches are common [27]: fitting data to a mathematical function or averaging the data. The data was first smoothed by averaging every 15 raw data and subsequently, the tangent derivatives of stress-strain curve (tangent drained bulk modulus) was calculated ($K_d = \frac{\partial P_c}{\partial \varepsilon_b}$) and were fitted to the functions of the form presented of Eq.13. The data analysing was aimed at determining the pressure dependence of porosity and permeability and relating them through the poroelastic and crack closure theories. First and second derivative of stress-strain curves were obtained, and the porosity and permeability were calculated.

The capillary (drainage) system was modified to minimize the thermal effects on stainless capillary tubes (Fig.1). A part of capillary tubes sits inside the triaxial cell and the other part connects the triaxial cell to the pumps. Three thermocouples were employed, two were placed close to the upper and lower part of the sample within the triaxial cell and one thermocouple was placed outside the triaxial cell to measure the atmospheric temperature. Inside the cell, a uniform temperature distribution was a reasonable assumption. The temperature measurement uncertainty was determined by relative error, the ratio between standard deviation $\sigma(T)$ and the average measured temperature $\overline{T}$ (see Table 2). The injected fluid was brought to the sample temperature by placing a longer spiral shape capillary within the chamber. However, a temperature distribution was established at capillary tubes outside, as the triaxial cell temperature and surrounding temperature stayed constant. In order to minimize this temperature distribution effect, the heat

transfer surface area was extended by employing fins and a spring shaped tube (see Figure 1).

Table 2: The uncertainty in temperature measurement was characterized by relative error [%], the ratio between standard deviation $\sigma(T)$ and the average measured temperature $\overline{T}$.

Temperature	Loading			Unloading		
[°C]	$\overline{T}$	$\sigma(T)$	[%]	$\overline{T}$	$\sigma(T)$	[%]
30	31.5	0.3	1.0	30.7	0.2	0.8
60	59.5	0.1	0.2	58.8	0.1	0.2
90	89.7	0.2	0.2	89.0	0.2	0.2
120	120.0	0.4	0.3	119.3	0.3	0.2
140	139.4	0.9	0.7	139.4	0.3	0.2

5 Experimental results

A drained jacketed test and a permeability measurement test (see Table 1) were performed. The porosity change was calculated by utilizing poroelastic theory and permeability was calculated by employing Darcy's law.

5.1 Porosity change

The porosity change was calculated by employing Eq.7. The tangent derivative of stress-strain curve was providing the tangent bulk modulus. The stress-strain curves were measured while performing jacketed test and permeability test. The stress-strain curves while flowing water through the

sample (Figure 2) showed that Flechtinger sandstone suffered from inelastic deformation. That is, the stress-strain curves showed non recoverable strain after each pressure cycle. The maximum inelastic strain was observant at °C. Table 3 summarize the inelastic strains and quantifies the consequent porosity reduction. It was assumed that inelastic bulk strain ε_b^{in} and pore strain are equal and the initial porosity was corrected for inelastic deformation in both samples ($V_p = V_p^i - \varepsilon_b^{in} \times V_p^i$). V_p^i is the initial pore volume at the beginning of each cycle.

The porosity change, calculated at drained conditions was compared with porosity change while flowing water through the sample. Both specimens showed a compatible porosity evolution (Fig.3). Therefore, porosity change was evaluated by employing tangent drained bulk (first derivative of stress-strain curve) while flowing water through the rock and using stress-strain curves plotted in Figure 2. The porosity of Flechtinger sandstone decreases with increasing effective pressure and after each pressure cycle (Table 3). The rate of porosity change with pressure was as low as 0.055 $[\%]/[MPa]$.

Table 3: The inelastic deformation of Flechtinger sandstone.

Temperature [°C]	Bulk inelastic strain [-]$\times 10^{-4}$	Porosity reduction [-]$\times 10^{-4}$	Porosity [%]
30	1.8	1.6	10.68
60	19	17	10.66
90	8.0	7.2	10.50
120	9.3	8.4	10.42
140	3.8	3.4	10.33

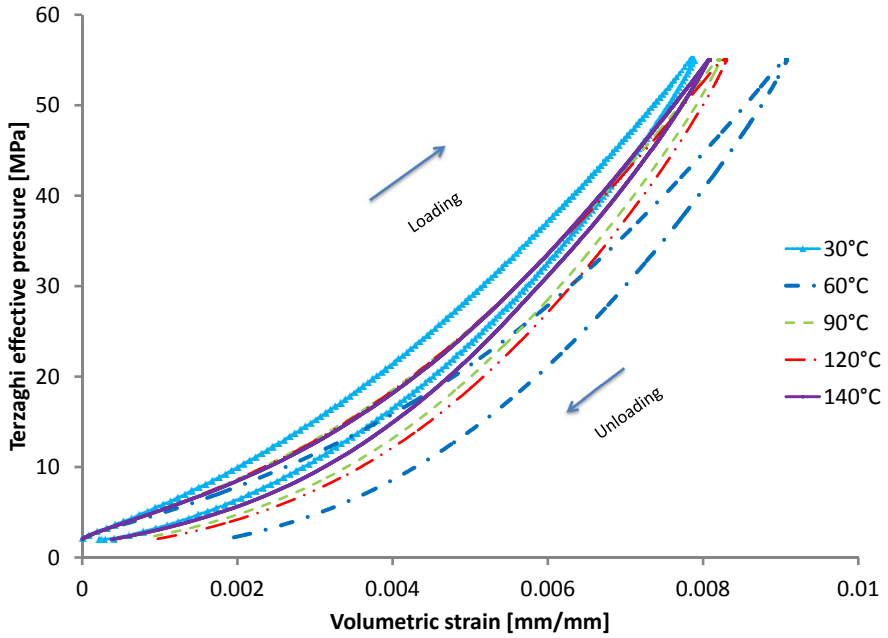

Figure 2: Terzaghi effective pressure versus volumetric strain. The downstream pore pressure was maintained constant at a value of 1 MPa and confining pressure was cycled.

5.2 Bulk modulus and crack porosity

The deformation of the specimen (FLG06) while performing the permeability test was captured by one axial and two lateral extensometers. The derivatives of stress-strain curve ($K_d = \frac{\partial P_c}{\partial \varepsilon_b}$) was calculated by numerical differentiation of neighboring data points and plotted as a function of mean effective pressure, the difference between confining pressure and average pore pressure within the sample. The strain measurement accuracy meets the requirement for calibration according to ISO 9513 class 0.5, where the strain measurement accuracy is $\pm$ 0.5% of reading or $\pm$ 1μm of the indicated value, whichever is

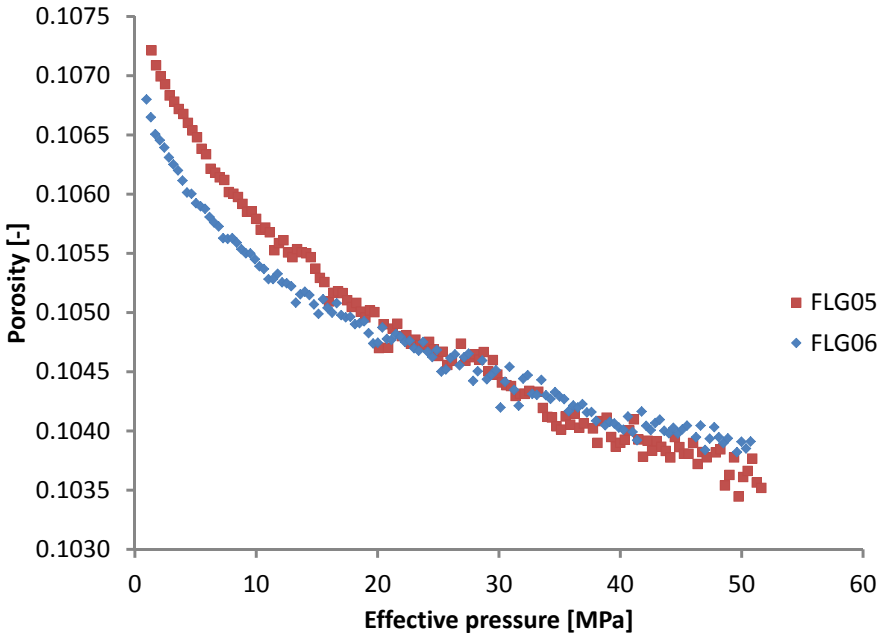

Figure 3: Porosity evolution as a function of effective pressure at drained and flowing conditions.

larger. The pressure measurement was quite precise with 0.001 MPa deviation. The error involved in calculating drained bulk modulus was estimated by Eq.24 to be approximately 30 MPa.

$$\left(\frac{\Delta K_d}{K_d}\right)^2 = \left(\frac{\Delta P}{P}\right)^2 + \left(\frac{\Delta \varepsilon_b}{\varepsilon_b}\right)^2 \tag{24}$$

Having calculated the uncertainty in measurements of the bulk modulus, the porosity-measurement error can be defined by the total derivative of the Eq.7 or Eq.16:

$$\left(\frac{\Delta \phi}{\phi}\right)^2 = \left(\frac{\Delta K_d}{K_d}\right)^2 + \left(\frac{\Delta P}{P}\right)^2 \tag{25}$$

The error in porosity measurement was estimated to be 3×10^{-4} (Eq.25). Afterwards, the data was fitted to the functions of the form suggested by Zimmerman (1991) and model parameters were derived by the least squares method where the overall solution minimizes the sum of the squares of the errors made at each data point. Figure 4 shows that the modeled bulk modulus adequately estimates the experimental data. A crossplot of Figure 4 was obtained (for all temperatures) by cutting the best fitting surface which was interpolated through data points, at different pressure levels. Figure 5 presents the evolution of bulk modulus due to temperature and the applied cyclic load. The bulk modulus slightly decreased with increasing temperature at low pressures and lightly increased with temperature at high pressures.

The solid matrix parameters, solid bulk modulus and Poisson's ratio of the Flechtinger sandstone, were calculated by the Voigt-Reuss-Hill average to be 41.2 GPa and 0.131, respectively (Hassanzadegan et al., 2012). The table 4 summarize the loading bulk modulus parameters and crack porosity at different loading paths and temperatures. A 50% increase in crack porosity was occurred at 60 °C. The characteristic closure pressure decreased after 60 °C pressure cycle. The value of the relaxed bulk modulus parameter K_d^i decreased after each pressure cycle and with increasing temperature (except from 60 °C), however the confined bulk modulus parameter was fluctuating. The table 5 summarize the unloading bulk modulus parameters and crack porosity. The value of K_d^∞ increased after each pressure cycle and with increasing temperature (except from 140 °C). The loading and unloading

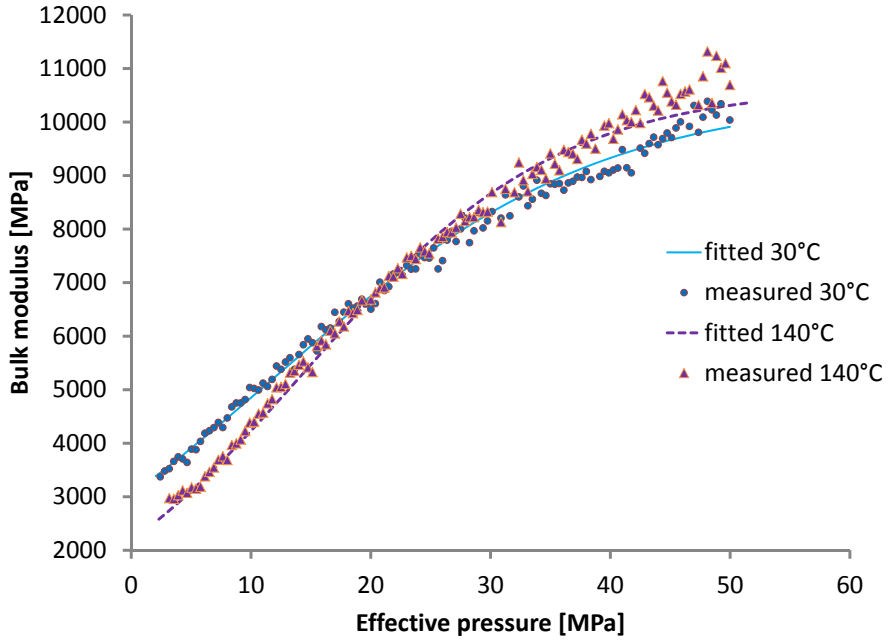

Figure 4: Loading bulk modulus as a function of effective pressure at 30 and 140 °C. The experimental data and modeled bulk modulus (Eq.13) fit adequately.

values of K_d^∞ were in the same range. The unloading parameters ϕ_c, $\hat{P}$ and K_d^i were smaller than those of loading path. Moreover, table 2 presents the average value of measured temperature at loading and unloading paths and its standard deviation.

Figure 6 compares the spectrums of the crack porosity function at loading and unloading paths. The Morlier's method was employed to determine the crack porosity function. At unloading path the maximum of $C(a)$ was shifted towards the smaller values of the aspect ratio. The maximum value at unloading spectrum was approximately two times of the loading one.

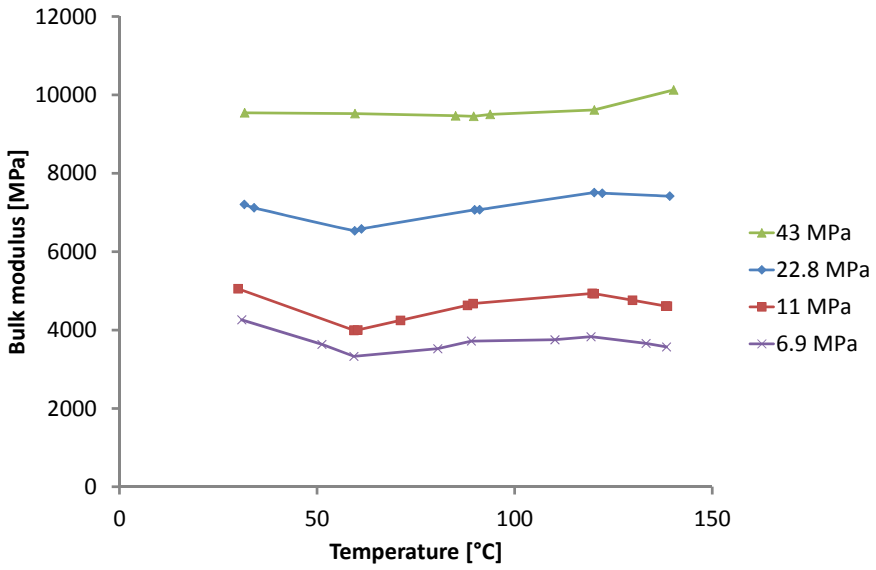

Figure 5: Bulk modulus as a function of temperature. A crossplot of Figure 4 shows the evolution of bulk modulus due to temperature and the applied cyclic load at different pressure levels. The new data points were obtained by interpolation.

Figure 7 shows loading spectrum of aspect ratio at different temperatures. At loading path, the maximum value of $C(a)$ was increased with increasing the temperature, except from the 60°C spectrum. Figure 8 displays the unloading spectrum of aspect ratio at given temperatures. The maximum value of function $C(a)$ was shifted towards smaller value of a in comparison to loading path and the maximum value of $C(a)$ function increased with increasing the temperature except from the 60 °C spectrum.

Table 4: Loading bulk modulus parameters at given temperatures.

Temperature	K_d^∞	K_d^i	$\hat{P}$	ϕ_{crack}
[°C]	[GPa]	[GPa]	[MPa]	[-]
30	10.51	3.05	13.49	0.0031
60	10.73	2.24	13.01	0.0046
90	10.25	2.37	11.44	0.0037
120	9.84	2.32	9.95	0.0033
140	10.68	2.18	10.64	0.0039

Table 5: Unloading bulk modulus parameters at given temperatures.

Temperature	K_d^∞	K_d^i	$\hat{P}$	ϕ_{crack}
[°C]	[GPa]	[GPa]	[MPa]	[-]
30	10.06	1.98	6.68	0.0027
60	10.56	2.23	7.85	0.0028
90	10.94	1.99	7.63	0.0031
120	10.97	1.95	7.41	0.0031
140	10.90	1.91	7.43	0.0032

5.3 Permeability

Permeability was measured at a constant flow rate of 0.02 ml/min and downstream pore pressure was kept constant at 1 MPa. The permeability was calculated by reading the pressure drop across the pressure transducer and employing Darcy's law (Eq.1). The permeability values are compatible with those reported by Blöcher et al. (2009). The relative precision error of permeability measurement, the ratio between standard deviation and average value, was calculated at a constant effective pressure, flow rate and temperature. The standard deviation, average value and relative error were calculated to

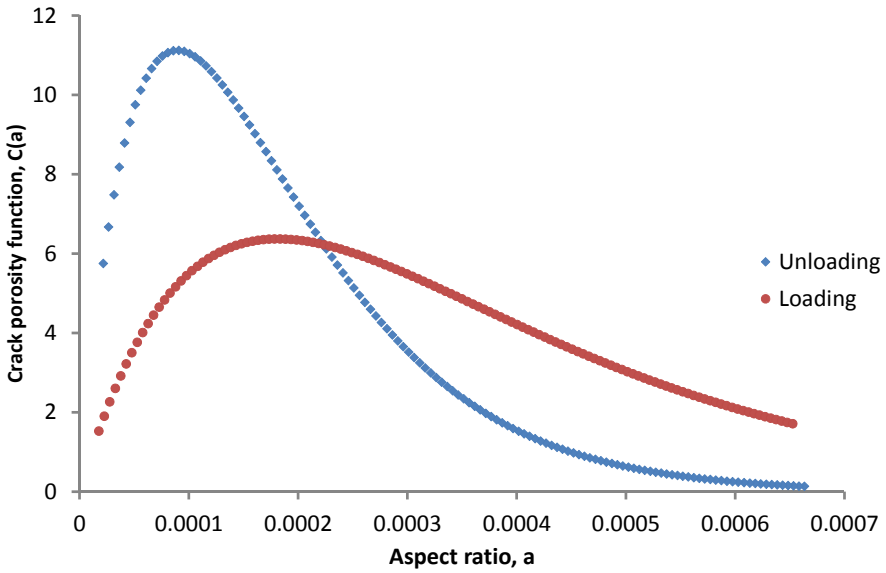

Figure 6: The loading and unloading aspect ratio distribution function of Flechtinger sandstone, as computed by Morlier's method at 30°C.

be 9.5×10^{-5}, 0.0253 and 0.38 %, respectively. The viscosity of water was corrected for temperature at 1 MPa. Figure 9 shows a good match between measured and the estimated permeability (Eq.22).

Figure 9 presents the loading permeability evolution as a function of mean effective pressure, the difference between confining pressure and average pore pressure within the sample. Permeability was decreasing with increasing effective pressure. The loading permeability decreased with increasing temperature and after first and second pressure cycles (30 and 60 °C) and slightly increased with increasing temperature and after (90 and 120 °C) pressure cycles. The rate of permeability change was high at relaxed state and permeability linearly decreased with increasing pressure at confined state. The

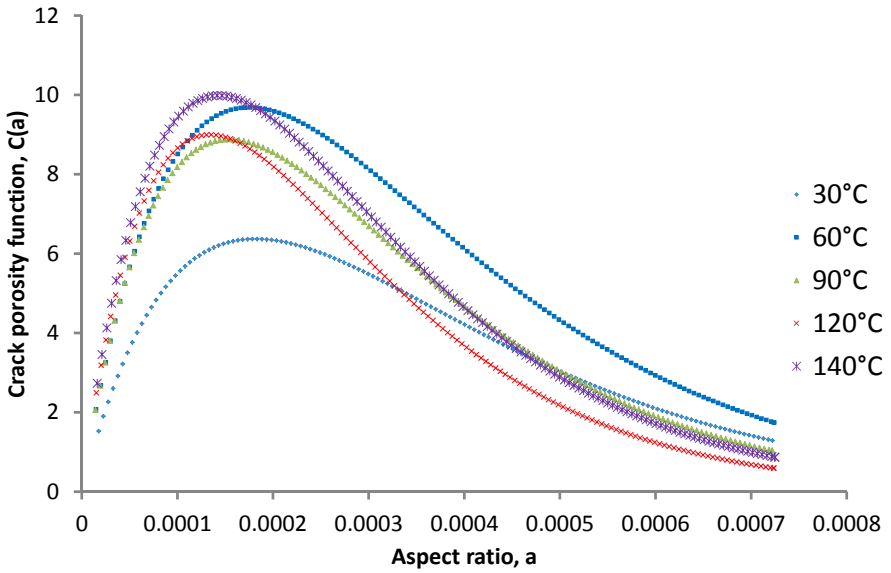

Figure 7: The loading aspect ratio distribution function of Flechtinger sandstone at different temperatures.

experimental permeability data were fitted to proposed model (section 3) and the validity of the model was confirmed by predicting appropriately the permeability evolution.

Figure 10 shows the unloading permeability evolution. The unloading permeability at 30 °C is partly presented due to the noise in the data. The unloading permeability was lower than loading permeability and was nonlinear at relaxed state, effective pressures lower than characteristic pressure, and was linear or approximately constant at confined state. The unloading permeability slightly increased with increasing temperature and after 30 °C pressure cycle and enormously decreased after 60 °C pressure cycle. The unloading permeability increased with increasing temperature and after 90 and

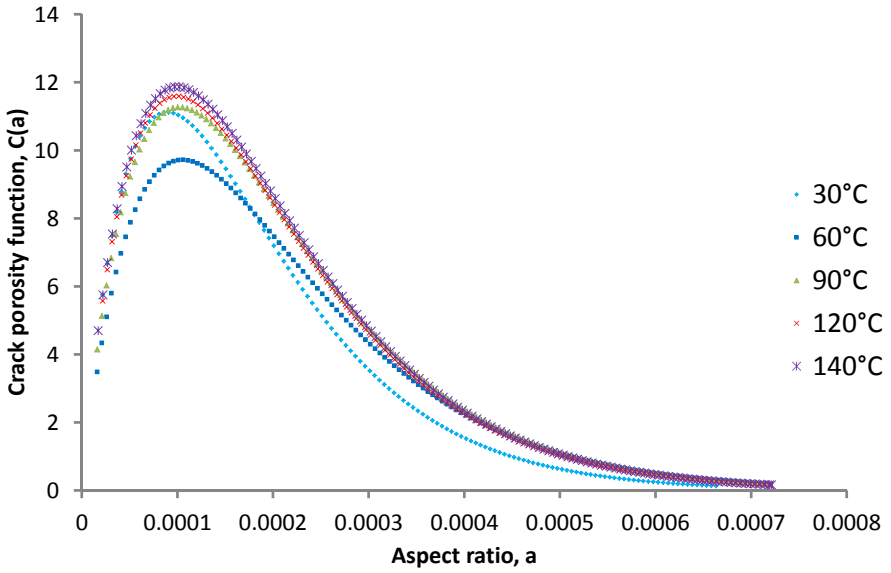

Figure 8: The unloading aspect ratio distribution function of Flechtinger sandstone at different temperatures.

120 °C pressure cycles. A crossplot of Figure 10 was obtained by cutting the best fitting surface at different pressure levels. The permeability decreased significantly up to 90 °C and slightly increased afterwards.

The terms $\hat{P}\left(\frac{\partial k}{\partial \phi}\right)$ and $k(P^{\infty})$ were obtained as best fitting parameters of Eq.23 and the Kozeny-Carman term $c_1 d^2$ was calculated. Then, assuming a constant geometric factor c_1 of $\frac{1000}{180} \times \frac{9}{4} = 12.5$ (Bear, 1988), the characteristic length d was calculated by employing Eq.4 (see Table 6). In general, the quality of match for unloading path was better than loading path (see Figure 10). The obtained confined state pressures P^{∞}, the Kozeny-Carman term $c_1 d^2$ and the characteristic length d at loading path were higher than unloading path. The loading high-pressure permeabilities $k(P^{\infty})$ were higher

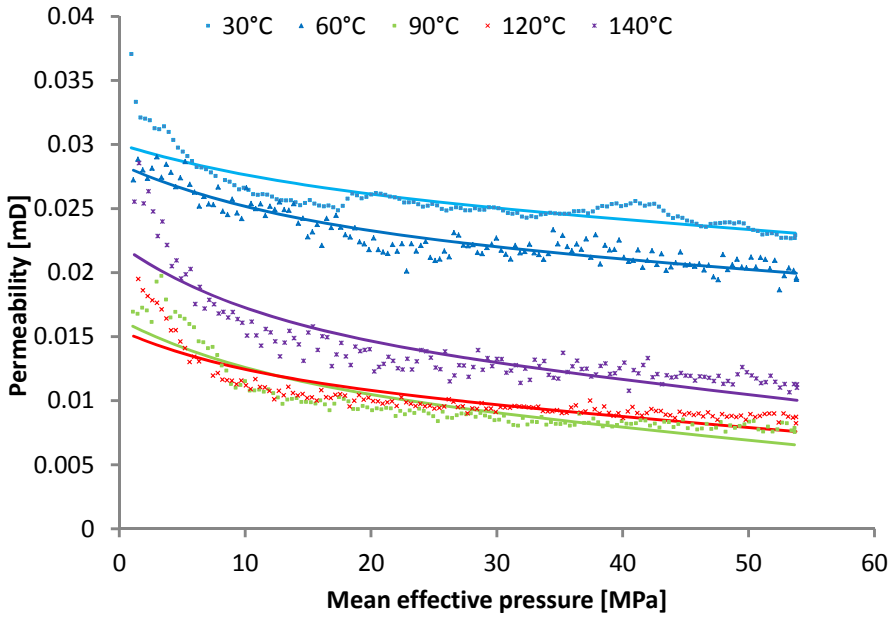

Figure 9: The loading permeability as a function of effective pressure and temperature. The solid lines show the matched permeability and scattered data points are experimental data.

than unloading ones at 30 and 60 °C, however the loading high-pressure permeabilities were lower at 90, 120 and 140 °C.

6 Interpretation and discussion

Three types of stress-permeability relations have been distinguished by David et al. (1994) and the mechanisms involved have been described: 1-low porosity crystalline rocks where the cracks are dominant, 2-porous clastic rocks where the relative movement of grains result in a decrease of permeability, and 3-grain crushing in unconsolidated material at high pressures.

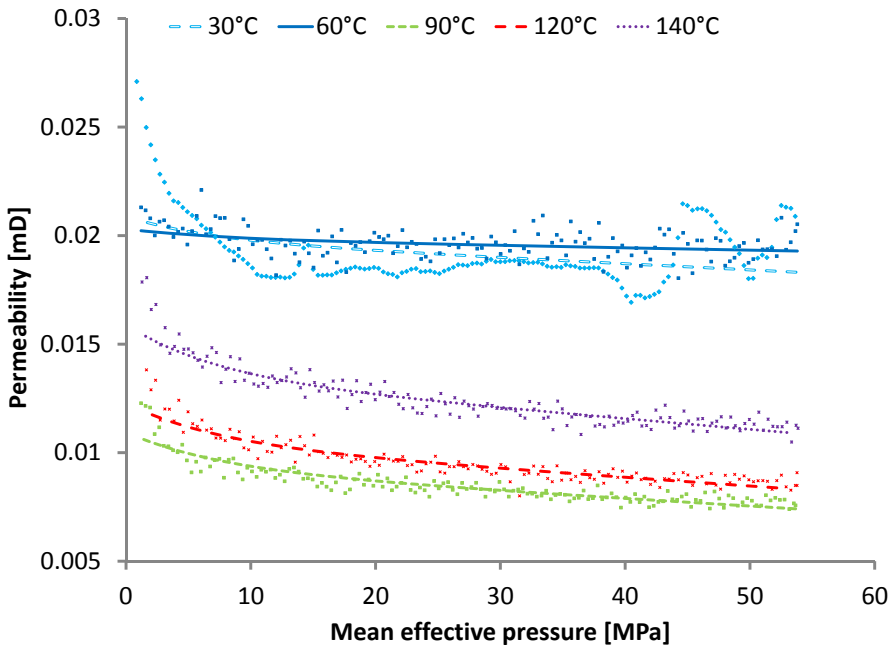

Figure 10: The unloading permeability as a function of effective pressure and temperature. The solid lines show the matched permeability and scattered data points are experimental data.

The effects of applied pressure on the permeability depends on the pore geometry and the degree of connectivity between pores. The effect of pressure is not the same for all pore geometries, the flat pores close easily when the pressure is applied, however the equant pores (high aspect ratio pores) are stiffer. While the crack porosity had a little contribution in total porosity of Flechtinger sandstone, but the cracks provided the interconnections between pores and fluid pathways. According to Guéguen and Palciauskas (1994) the closure of the cracks depends on the elastic processes up to a certain value of pressure, after which the crack roughness and stiffness of equant pores

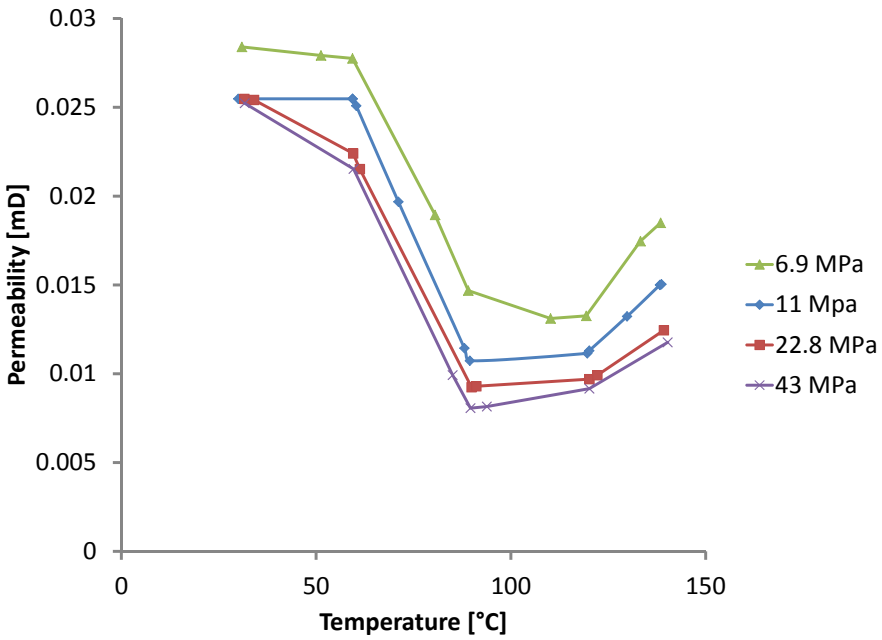

Figure 11: Permeability as a function of temperature at loading path. A crossplot of Figure 9 presents the permeability evolution. The new data points were obtained by interpolation.

preserve the permeability. In contrast, the crack volume is relatively a small part of the total porosity and the total porosity is governed by other than that caused by narrow cracks (Walsh, 1980).

Guéguen and Dienes (1996) presented two simple models, using 1D and 2D objects, pipes and cracks, respectively. The pore micro-structure was determined by statistical distribution of three parameters: average pipe (crack) length, average pipe radius (crack aperture) and average pipe (crack) spacing. The introduced permeability model relates the microstructure of porosity, strain and permeability through the key concept of effective pressure. The

Table 6: The permeability fitting parameters. The Kozeny-Carman term $c_1 d^2$ and high-pressure permeability $k(P^\infty)$ were obtained as best fitting parameters of Eq.23.

	Loading				Unloading			
Temperature [°C]	P^∞ [MPa]	$c_1 d^2 \times 10^{-8}$ $[m^2]$	d [μm]	$k(P^\infty)$ [mD]	P^∞ [MPa]	$c_1 d^2 \times 10^{-8}$ $[m^2]$	d [μm]	$k(P^\infty)$ [mD]
30	52.1	2.5	45	0.0232	31.7	1.1	29	0.0180
60	53.8	2.8	47	0.0199	35.1	0.4	19	0.0195
90	51.8	1.4	33	0.0067	38.2	1.5	35	0.0080
120	45.3	1.2	31	0.0083	36.8	0.6	21	0.0090
140	46.4	1.8	38	0.0109	37.5	0.8	26	0.0117

common approach to model pressure-dependence of the rock bulk modulus is to introduce a crack aspect ratio distribution of penny-shaped cracks (Walsh, 1980). The Flechtinger sandstone was assumed to be embedded by equant pores and penny-shaped cracks in a solid phase. The spherical pores (equant pores) are the stiffest type of the pores and could be assumed non-closable under typical elastic stress. The new model predicts the permeability evolution from a relaxed state, where the low aspect ratio cracks are open, to a confined state, where the cracks gradually close. The presented model introduce a characteristic closure pressure at which a transition from relaxed state to a confined state will occur. At relaxed state, pressures lower than characteristic closure pressure, the rock is more compliant and becomes stiffer with increasing effective pressure (confined state).

The presented model describe the nonlinear behavior of stress-strain curve

by crack closure, however does not include the other nonlinearities such as Skempton effect (increase in pore pressure due to the applied confining pressure). Moreover, the presented model assumes a quasi-static deformation and does not include the transient response, where the pore pressure diffusion is coupled with change in mass content.

The permeability model is compatible with percolation concept where the occupancy probability p is proportional to the crack porosity ϕ_c and inversely proportional to the aspect ratio a (Guéguen and Palciauskas, 1994). The Eq.15 presents a differential form of the occupancy probability. Both permeability and bulk modulus were assumed to be proportional to the cumulative population of open cracks which their probability density function can be derived by normalizing Eq.15. A relaxed bulk modulus, a confined bulk modulus and a characteristic closure pressure (aspect ratio) are the key parameters that characterize the bulk modulus and permeability model. At relaxed state where the most cracks are open the probability to have a connected network is high and by increasing the pressure the probability of having a connected fluid path decreases.

The exponential bulk modulus functions were fitted to experimentally measured tangent drained bulk modulus (Fig.4). At low effective pressures, both cracks (low aspect ratio pores) and equant dimension pores affect the elastic moduli and the rock exhibit compliant behavior, where the pressure dependence of bulk modulus is large. However, by increasing the confining pressure the cracks close and the spherical pores do not. The quality of the

match is convenient for middle and high pressures, however at low pressures a deviation can be observed. At high pressures and temperatures, the rock is stiffer than predicted which can be assigned to inelastic behavior of the Flechtinger sandstone. The inelastic behavior of the rock was observed to be higher during 60 °C pressure cycle (see Table 3).

Figure 6 shows that the maximum value of crack porosity function is moving towards the higher aspect ratio at loading path. Accordingly, the loading characteristic closure pressure is higher than unloading characteristic closure pressure. That is, a higher effective pressure at loading path is required in comparison to unloading path to close the high density cracks (the cracks with a certain aspect ratio which have the highest population). It confirms that the unloading moduli can be approximated to be elastic moduli at the initial part of unloading path where the most of the cracks are closed.

The range of aspect ratio values is compatible with those derived for Boise, Berea and Bandera sandstones (Zimmerman, 1991). The small value of aspect ratios can be explained by the fact that crack closure theory does not consider the interaction between cracks. Moreover, as presented in Eq.8, the crack radius appears in third power. That is, a few long cracks may strongly affect the rock behavior. David and Zimmerman (2012) reported an order of magnitudes higher aspect ratios for Vosgas and Fontainbleau sandstone, albeit the samples were subjected to a high confining pressure of 280 MPa.

The discrepancy in spectrums at loading and unloading paths, could ex-

plain the hysteresis in permeability evolution as observed here and by Bernabe (1986, 1987). The number of cracks which are open to fluid flow at loading and unloading paths at a same pressure is different. At unloading path, more cracks are open at relaxed state while at loading path the number of cracks which are open at low or middle range pressure is higher. At unloading path, the density of low aspect ratio cracks is high at relaxed state (unloading maximum value) while at loading path, the density of higher aspect ratio cracks exceeds the unloading one (Fig. 6). The total crack porosity at loading path is higher than unloading path (see Tables 4 and 5). Furthermore, the unloading spectrum of aspect ratio follows a special trend with respect to temperature and the maximum value of aspect ratio distribution function increases with temperature (Fig.8). The crack porosity increased with temperature and after each pressure cycle, however the crack porosity change was close to the calculated uncertainty (see Table 5). Creation of new cracks due to applied thermal and mechanical loads could explain the increase in crack porosity and observed permeability changes. In addition, the calculated characteristic lengths d and Kozeny-Carman term $c_1 d^2$ were lower at unloading paths than loading paths (see Table 6).

Figures 9 and 10 show that loading and unloading permeability decreased after each pressure cycle and with increasing temperature. The inelastic behavior of Flechtinger sandstone suggests that pore collapse or compaction of grains lowers the total porosity and affects on how easily fluid flows within the rock. This is in agreement with what has been observed by Fortin et al.

(2005). Fortin et al. (2005) concluded that inelastic compaction leads to a decrease in porosity and permeability, due to pore collapse. The permeability of Flechtinger sandstone decreased considerably after 60 °C pressure cycle where the highest amount of inelastic strain was observed (see Table 3). In contrast, the thermo-mechanical loading increased the crack porosity (see Table 5) and consequently affect on fluid flow.

7 Conclusion

A new permeability model was derived from the basic principles underlying the theories of poroelasticity and crack closure. The strain (bulk modulus) was related to microstructure of porosity and permeability was related to strain (bulk modulus). The first and second derivative of stress-strain curves were employed to connect permeability and microstructure of porosity. The loading and unloading aspect ratio distribution described the hysteresis in permeability during loading and unloading paths. The loading permeability decreased with increasing temperature and after each pressure cycle.

Measurements of the mechanical behavior of the Flechtinger sandstone showed that stress-strain curves were nonlinear and not all the strains were recovered after unloading. The pressure dependence of the bulk modulus and nonlinearity in stress-strain curves was assigned to presence of cracks. The permeability was governed by cracks where the cracks not only provide pathways to fluid flow but also guaranty the inter-connection between pores.

The permeability decreased with increasing effective pressure and after each pressure cycle. It was nonlinear at relaxed state (low effective pressures) and linear at confined state (high effective pressures). In contrast, the unloading crack porosity was slightly increased. It can be concluded that a competition between Thermo-mechanical crack creation, and inelastic deformation of the rock governs the permeability evolution under cyclic loading.

Acknowledgments

The authors would like to gratitude Liane Liebeskind for Laboratory assistance. Moreover, the authors would like to thank the reviewers for their constructive and valuable comments that helped to improve the manuscript. This work has been performed in the framework of the GeoEn-Phase 2 project and funded by the Federal Ministry of Education and Research [BMBF, 03G0767A].

References

Bear, J. (1988). *Dynamics of Fluids in Porous Media*. Dover Books on Physics and Chemistry. Dover.

Bernabe, Y. (1986). The effective pressure law for permeability in chelmsford granite and barre granite. *International Journal of Rock Mechanics and Mining Sciences & Geomechanics Abstracts*, 23(3):267–275.

Bernabe, Y. (1987). The effective pressure law for permeability during pore pressure and confining pressure cycling of several crystalline rocks. *J. Geophys. Res.*, 92:649–657.

Biot, M. (1956). General solutions of the equations of elasticity and consolidation for a porous material. *Journal of Applied Mechanics*, 78:91–96.

Biot, M. A. (1941). General theory of three-dimensional consolidation. *J. Appl. Phys.*, 12(2):155–164.

Biot, M. A. (1973). Nonlinear and semilinear rheology of porous solids. *Journal of Geophysical Research*, 78:4924–4937.

Blöcher, G., Zimmermann, G., and Milsch, H. (2009). Impact of poroelastic response of sandstones on geothermal power production. *Pure and Applied Geophysics*, 166(5-7): 1089–1106.

Brace, W. (1980). Permeability of crystalline and argillaceous rocks. *International Journal of Rock Mechanics and Mining Sciences & Geomechanics Abstracts*, 17(5):241 – 251.

Brace, W. F. (1978). Volume changes during fracture and frictional sliding: A review. *Pure and Applied Geophysics*, 116:603–614.

Carman, P. (1956). *Flow of gases through porous media*. Butterworths Scientific Publications.

Carroll, M. (1980). Mechanical response of fluid suturated porous materials. In *Theoretical and Applied Mechanics, Proc. 15th Int. Congress of Theoretical and Applied Mechanics, Toronto, August 1723, F. P. J. Rimrott and B. Tabarrok, eds., North-Holland, Amsterdam*, pages 251–262.

Carroll, M. M. and Katsube, N. (1983). The role of terzaghi effective stress in linearly elastic deformation. *Journal of Energy Resources Technology-Transactions of the Asme*, 105(4):509–511.

David, C., Menendez, B., Zhu, W., and f. Wong, T. (2001). Mechanical compaction, microstructures and permeability evolution in sandstones. *Physics and Chemistry of the Earth, Part A: Solid Earth and Geodesy*, 26(12):45–51.

David, C., Wong, T.-F., Zhu, W., and Zhang, J. (1994). Laboratory measurement of compaction-induced permeability change in porous rocks: Implications for the generation and maintenance of pore pressure excess in the crust. *Pure and Applied Geophysics*, 143:425–456.

David, E. C., and Zimmerman, R. W. (2012). Pore structure model for elastic wave velocities in fluid-saturated sandstones. *Journal of Geophysical Research: Solid Earth*, 117:2156-2202.

Detournay, E. and Cheng, A. H.-D. (1993). *Fundamentals of poroelasticity. In Comprehensive Rock Engineering: Principles, Practice and Projects*, volume 2, chapter 5, pages 113 –171. Pergamon Press.

Fortin, J., Schubnel, A., and Guéguen, Y. (2005). Elastic wave velocities and permeability evolution during compaction of bleurswiller sandstone. *International Journal of Rock Mechanics and Mining Sciences*, 42(78):873 – 889.

Guéguen, Y., Gavrilenko, P., and Le Ravalec, M. (1996). Scales of rock permeability. *Surveys in Geophysics*, 17:245–263.

Guéguen, Y., and Dienes J. (1989). Transport properties of rocks from statistics and percolation. *Mathematical Geology*, 21(1):1–13.

Guéguen, Y. and Palciauskas V. (1994). Introduction to the Physics of Rocks. Princeton University Press.

Hassanzadegan, A., Blöcher, G., Milsch, H., Urpi, L. and Zimmermann G. (2013). The Effects of Temperature and Pressure on the Porosity Evolution of Flechtinger Sandstone *Rock Mechanics and Rock Engineering*, doi=10.1007/s00603-013-0401-z.

Hassanzadegan, A., Blöcher, G., Zimmermann, G., and Milsch, H. (2012). Thermoporoelastic properties of Flechtinger sandstone. *International Journal of Rock Mechanics and Mining Sciences*, 49(0):94 –104.

Hassanzadegan, A., Blöcher, G., Zimmermann, G., Milsch, H., and Moeck, I. (2011). Induced stress in a geothermal doublet system. In *Thirty-Sixth Workshop on Geothermal Reservoir Engineering, Stanford University, Stanford, California, SGP-TR-191*, pages 1–1.

Jaeger, J., Cook, N., and Zimmerman, R. (2007). *Fundamentals of Rock Mechanics*. Blackwell Pub.

Keaney, G., P.G.Meredith, and Murrell, S. (1988). Laboratory study of permeability evolution in a tight sandstone under non-hydrostatic stress conditions. *SPE/ISRM Rock Mechanics in Petroleum Engineering*, 47265.

Lemmon, E., Huber, M., and Mclinden, M. (2007). *Reference fluid thermodynamic and transport propertiesrefprop*. version 8.0, National Institute of Standards and Technology, Gaithersburg, NIST Standard Reference Database 23.

Morlier, P. (1971). Description de l'ètat de fissuration d'une roche à partir d'essais non-destructifs simples. *Rock Mechanics and Rock Engineering*, 3:125–138.

Palciauskas, V. and Domenico, P. A. (1982). Characterization of drained and undrained response of thermally loaded repository rocks. *Water Resources Research*, 18(2):281–290.

Rice, J. R. and Cleary, M. P. (1976). Some basic stress diffusion solutions for fluid-saturated elastic porous media with compressible constituents. *Reviews Of Geophysics And Space Physics*, 14(2):227–241.

J. Sarout (2012). Impact of pore space topology on permeability, cut-off frequencies and validity of wave propagation theories. *Geophysical Journal International* 189: 481–492

Scheidegger, A.E. (1974). The physics of flow through porous media. University of Toronto Press.

Sisavath, S., Jing, X., and Zimmerman, R. (2000). Effect of stress on the hydraulic conductivity of rock pores. *Physics and Chemistry of the Earth, Part A: Solid Earth and Geodesy*, 25(2):163 – 168.

Walsh, J. B. (1965). The effect of cracks on the compressibility of rock. *J. Geophys. Res*, 70(2):381–389.

Walsh, J. B. (1980). Static deformation of rock. *Journal Of The Engineering Mechanics Division*, 106:1005–1019.

Zimmerman, R. (1991). *Compressibility of Sandstones*. Developments in Petroleum Science. Elsevier.

Zoback, M. and Byerlee, J. (1975). Permeability and effective stress. *American Association Of Petroleum Geologists Bulletin*, 59:154–158.